

Deep Learning Based Detection of Enlarged Perivascular Spaces on Brain MRI

Tanweer Rashid^{a,b,§}, Hangfan Liu^{a,b,§}, Jeffrey B. Ware^c, Karl Li^a, Jose Rafael Romero^d, Elyas Fadaee^a, Ilya M. Nasrallah^{b,c}, Saima Hilal^e, R. Nick Bryan^{c,f}, Timothy M. Hughes^g, Christos Davatzikos^c, Lenore Launer^h, Sudha Seshadri^a, Susan R. Heckbertⁱ, Mohamad Habes^{a,b,}*

^a*Neuroimage Analytics Laboratory and Biggs Institute Neuroimaging Core, Glenn Biggs Institute for Neurodegenerative Disorders, University of Texas Health Science Center at San Antonio, San Antonio, TX, USA*

^b*Center for Biomedical Image Computing and Analytics, University of Pennsylvania, Philadelphia, PA, USA*

^c*Department of Radiation Oncology, University of Pennsylvania, Philadelphia, PA, USA*

^d*Department of Neurology, School of Medicine, Boston University, Boston, MA, USA*

^e*Saw Swee Hock School of Public Health, National University of Singapore and National University Health System, Singapore*

^f*Department of Diagnostic Medicine, Dell Medical School, University of Texas at Austin, Austin, TX, USA*

^g*Department of Internal Medicine and Department of Epidemiology and Prevention, Wake Forest School of Medicine, Winston-Salem, NC, USA*

^h*Laboratory of Epidemiology and Population Sciences, National Institute on Aging, National Institutes of Health, Bethesda, MD, USA*

ⁱ*Department of Epidemiology and Cardiovascular Health Research Unit, University of Washington, Seattle, WA, USA*

[§]*Equal contributing first authors.*

^{*}*Corresponding author. E-mail address: habes@uthscsa.edu*

ABSTRACT

BACKGROUND AND PURPOSE: Deep learning has been demonstrated effective in many neuroimaging applications. However, in many scenarios, the number of imaging sequences capturing

information related to small vessel disease lesions is insufficient to support data-driven techniques. Additionally, cohort-based studies may not always have the optimal or essential imaging sequences for accurate lesion detection. Therefore, it is necessary to determine which imaging sequences are crucial for precise detection. This study introduces a novel deep learning framework to detect enlarged perivascular spaces (ePVS) and aims to find the optimal combination of MRI sequences for deep learning-based quantification.

MATERIALS AND METHODS: We implemented an effective lightweight U-Net adapted for ePVS detection and comprehensively investigated different combinations of information from SWI, FLAIR, T1-weighted (T1w), and T2-weighted (T2w) MRI sequences. The training data included 21 participants, which were randomly selected from the MESA cohort. Participants had ePVS 683 lesions on average. For T1w, T2w, and FLAIR images, the MESA study collected 3D isotropic MRI scans at six different sites with Siemens scanners. Our training data included participants from all these sites and all the scanner models, and the proposed model was applied to the whole brain instead of selective regions.

RESULTS: The experimental results showed that T2w MRI is the most important for accurate ePVS detection, and the incorporation of SWI, FLAIR and T1w MRI in the deep neural network had minor improvements in accuracy and resulted in the highest sensitivity and precision (sensitivity =0.82, precision =0.83). The proposed method achieved comparable accuracy at a minimal time cost compared to manual reading.

CONCLUSIONS: The proposed automated pipeline enables robust and time-efficient readings of ePVS from MR scans and demonstrates the importance of T2w MRI for ePVS detection and the potential benefits of using multimodal images. Furthermore, the model provides whole-brain maps of ePVS, enabling a better understanding of their clinical correlates compared to the clinical rating methods within only a couple of brain regions.

1. Introduction

Enlargement of perivascular, or Virchow-Robin, spaces^{1,2} can manifest cerebral small vessel disease and dysfunction of perivascular drainage routes. Perivascular spaces are fluid-filled spaces that surround arteries, arterioles, veins, and venules³ in the brain. They are generally microscopic but may become enlarged and visible with increasing age and/or pathologies, i.e., enlarged perivascular spaces (ePVS)²⁻⁵. Typically, ePVS appear as bright or hyperintense linear or curvilinear structures when running parallel to the imaging plane and ellipsoidal or dot-like when perpendicular to the imaging plane on T2-weighted (T2w) MRI^{2,3}. When perivascular spaces are enlarged, they become visible on routine structural MRI, typically with a diameter of less than 3mm. They can reach up to 10-20 mm in regions such as the basal ganglia³. While ePVS can be evaluated on T1-weighted (T1w) and T2w sequences, they are easier to visualize and quantify using T2w imaging^{6,7}.

Many detection/segmentation methods have been proposed^{5,7-10}, which rely on T2w exclusively for the detection/segmentation of ePVS. However, it is still unclear if models depending on a single modality such as T2w could account for similar-appearing brain lesions such as white matter hyperintensities (WMH), lacunes, and infarcts. WMH are hyperintense on T2w sequences and can appear as isointense or hypointense on T1w sequences; lacunes are round or ovoid subcortical fluid-filled cavities of between 3 mm and 15 mm in diameter, while infarcts are neuroimaging evidence of recent infarction in the territory of one perforating arteriole³.

In this paper, we aim to evaluate the feasibility and effectiveness of an automated deep learning-based method for segmenting ePVS using multiple MRI sequences from a subset of participants in the Multi-Ethnic Study of Atherosclerosis (MESA) cohort. The brain data

collected by the MESA Atrial Fibrillation (AFib) ¹¹⁻¹⁴ ancillary study at Exam 6 offer a unique and rich dataset of high-quality brain MRI at clinical field strength and high spatial resolution (1 mm isotropic images). We aim to evaluate the accuracy and reliability of ePVS segmentation in the presence or absence of T2w MRI and when T2w is combined with other MRI sequences. We used a variation of our method, previously developed using MESA brain MRI data for fully automated detection of cerebral microbleeds and non-hemorrhage iron deposits in the basal ganglia ¹⁵, and investigate the optimal strategy of combining information from SWI, FLAIR, T1w, and T2w MRI sequences. A set of ePVS segmentations by a human expert served as the gold standard for model training.

Automation is ideal in large cohort studies for feasibility, improved reproducibility, and reduced human error ¹⁶. Accurate and reliable methods are also essential for deriving rich datasets from large cohorts to study associations with demographic, cognitive, and vascular risk factors ¹⁷⁻¹⁹, or to refine the development of new methods ^{20,21}.

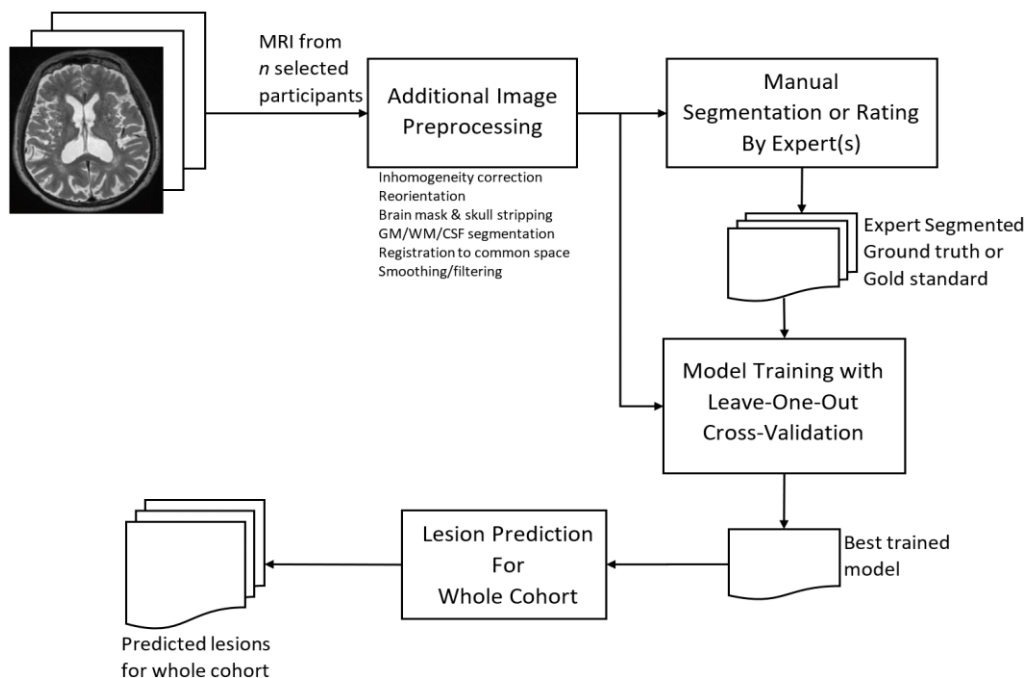


Fig. 1. Overview of the ePVS detection/segmentation procedure.

To our knowledge, this study is among the first to comprehensively evaluate multimodal imaging for ePVS detection with deep learning. The main contributions of this paper include the following:

1. Development of an effective deep learning scheme with data fusion for accurate ePVS segmentation.
2. Application of the proposed model to the whole brain instead of selective regions.
3. Investigation of the use of different sequences for optimal performance.

2. Related Works

Previous ePVS segmentation methods typically adopt conventional machine learning techniques such as vessel enhancement filters⁷ and support vector machines (SVM)²². Ballerini et al. trained a model on T2-contrast MR images⁷ and evaluated it by categorical scores⁶. González-Castro et al. applied an SVM classifier with a bag of visual words-based descriptors to

the T2-weighted MR images with a focus on the basal ganglia ²². Wang et al. developed a semi-automatic computational method that extracts ePVS on bilateral ovoid basal ganglia on intensity-normalized T2w MRI ⁹. Meanwhile, some works exploited handcrafted features as predictors. For example, Boespflug et al. used signal intensities and morphologic characterizations, including width, volume, and linearity ²³, while Ramirez et al. used set localized intensity thresholds for quantification of perivascular spaces ²⁴, and Zhang et al. proposed vascular feature based structured learning for 3-dimensional ePVS segmentation using T2w data ⁸. Besides, to facilitate these models, Sepehrband et al. combined T1- and T2w images to enhance PVS contrast and intensify visibility ²⁵.

With the recent success of deep learning techniques ^{21,26-28}, some deep neural network models were proposed for ePVS segmentation. For instance, Boutinaud et al. developed a deep learning algorithm based on an autoencoder and a U-shaped network for the 3-dimensional segmentation of ePVS in deep white matter and basal ganglia using T1-weighted MRI data ²⁹. Lian et al. proposed a fully convolutional neural network using 7T T2-weighted MRI for efficient segmentation of ePVS ¹⁰, Dubost et al. implemented separate convolutional neural networks for midbrain, hippocampi, basal ganglia, and centrum semiovale, trained on T2-contrast MRI to quantify PVS ³⁰, Sudre et al. redesigned the region-based convolutional neural networks model to jointly detect and characterize markers of age-related neurovascular changes ³¹. Jung et al. presented a deep 3-dimensional convolutional neural network with densely connected networks with skip connections for ePVS enhancement of 7T MRI ³². In general, these works did not investigate how to fully utilize different sources of information for improved ePVS detection on the whole brain based on deep data-driven techniques. Furthermore, these prior studies mostly used 7T MRI, which is highly experimental and not readily available. 3T MRI is more

conventional and widely available, so a deep learning model tailored for 3T MRI a more cost-effective choice.

3. Materials and Methods

The key point of the proposed scheme is a deep fusion of information from different MRI sequences. An overview of the whole procedure is summarized in Fig. 1. Standard image processing techniques were first applied to raw MRI data of different sequences from a subset of the MESA cohort, including inhomogeneity correction, reorientation, smoothing and filtering, brain masking and skull-stripping, followed by gray matter (GM), white matter (WM) and cerebrospinal fluid (CSF) segmentation. Then the participants' MRIs were registered to SWI. Preprocessed MRI data were manually segmented to obtain the ground truth used for model training with leave-one-out cross-validation.

3.1. Data

The training data included 21 participants, which were randomly selected from the MESA cohort. For T1w, T2w, and FLAIR images, the MESA study collected 3D isotropic MRI scans at six different sites with Siemens scanners (Skyra with a 20-channel head coil, Prisma and Prisma Fit with a 32-channel head coil). Our training data included participants from all these sites and all the scanner models, thus ensuring generalizability within the MESA cohort. The MRI scan parameters are shown in supplementary material Table S1.

The ages of the 21 participants range from 64 to 94 years, with an average of 78.7 years, and 12 of them are female. The average total number of individual lesions per participant is more than 683. The ePVS segmentation of these participants was performed by an experienced

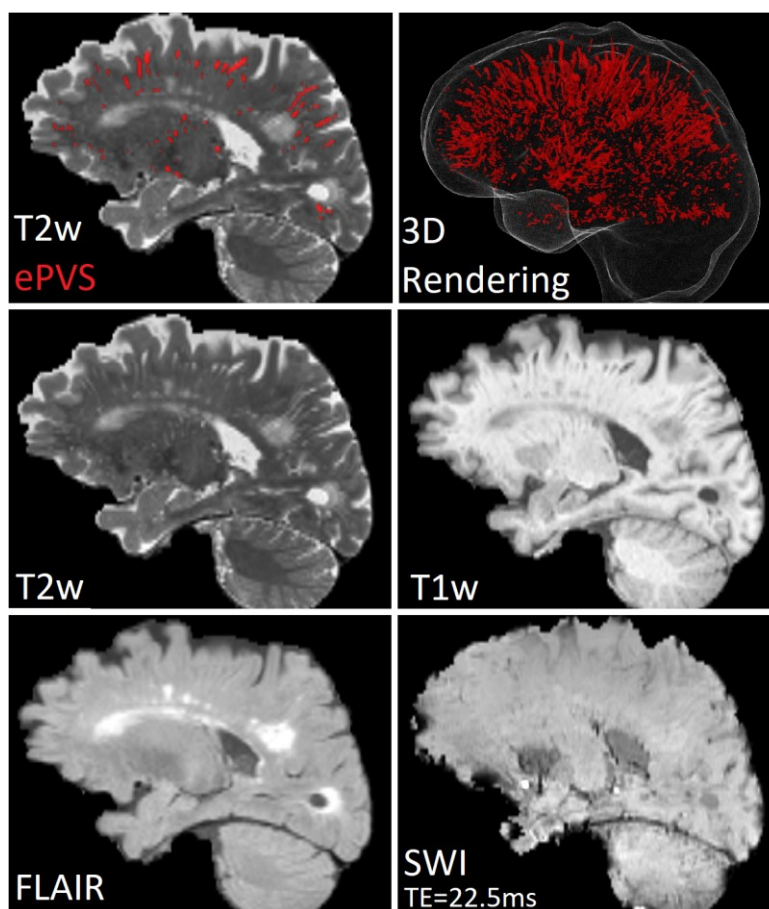


Fig. 2. Examples of ePVS in different MRI sequences.

radiologist (JBW) and served as ground truth for model training (see supplementary material Table S2). The average time to create the ground truth was ~ 24 hours per scan. The manual segmentation was performed using co-registered T2w, T1w, and FLAIR images to ensure a reduced likelihood of false positives such as WMH or lacunes³ being present in the ground truth. The average time needed to complete a manual segmentation was around 30 hours per participant. For model training and evaluation, we used FLAIR, SWI, T1w, and T2w images, which were reoriented, N4 bias corrected³³, and skull-stripped³⁴. The SWI phase mask was generated from the phase images using a high-pass filter of size 64 x 64 to remove artifacts, and the SWI was generated by multiplying the magnitude image with the phase mask³⁵. For the

creation of the reference annotation and machine-based inference, only the SWI image with the shortest echo time (TE=7.5 ms) was used since SWI acquired with longer echo times are noisier. Examples of ePVS on the different sequences are shown in Fig. 2. The MRI scans used in this study have a high spatial resolution, making it possible to detect small ePVS. However, in clinical settings, the slice thickness is larger to allow for less scan time, so small lesions occurring between slices may not be visible.

3.2. Deep Fusion of Different Sequences

Suppose $f_U: \mathbb{R}^{n \times S} \rightarrow \mathbb{R}^S$ is a nonlinear function with a set of learnable parameters U , where n is the number of MRI Sequences used, and S is the size of the images, f maps the n images to voxel-wise labels indicating whether the voxel contains ePVS or not. In this study, f_U is implemented as a multi-channel deep neural network¹⁵, a variation of the standard U-Net³⁶ and has been demonstrated superior to conventional U-Net for small lesions¹⁵. A typical U-Net comprises a down-sampling or encoding path and a symmetric up-sampling or decoding path. The down-sampling course consists of a series of convolutional blocks, normalization blocks, activation blocks, and pooling blocks. The up-sampling path consists of a series of convolutional blocks, normalization blocks, activation blocks, and transposes convolutional blocks. The feature maps of each corresponding down-sampling path and up-sampling path are concatenated.

The proposed scheme could perform a deep fusion of information from different sequences. The ePVS detection/segmentation model fuses information from T2w, SWI, FLAIR, and T1w images through the multi-channel U-Net. It was designed in a scalable manner, i.e., the network using T2 only was basically a single-channel U-Net, and can be easily expanded to include multiple sequences. The manual segmentations by the human expert were used to train the deep learning model using leave-one-out cross-validation. Specifically, in each iteration of the leave-

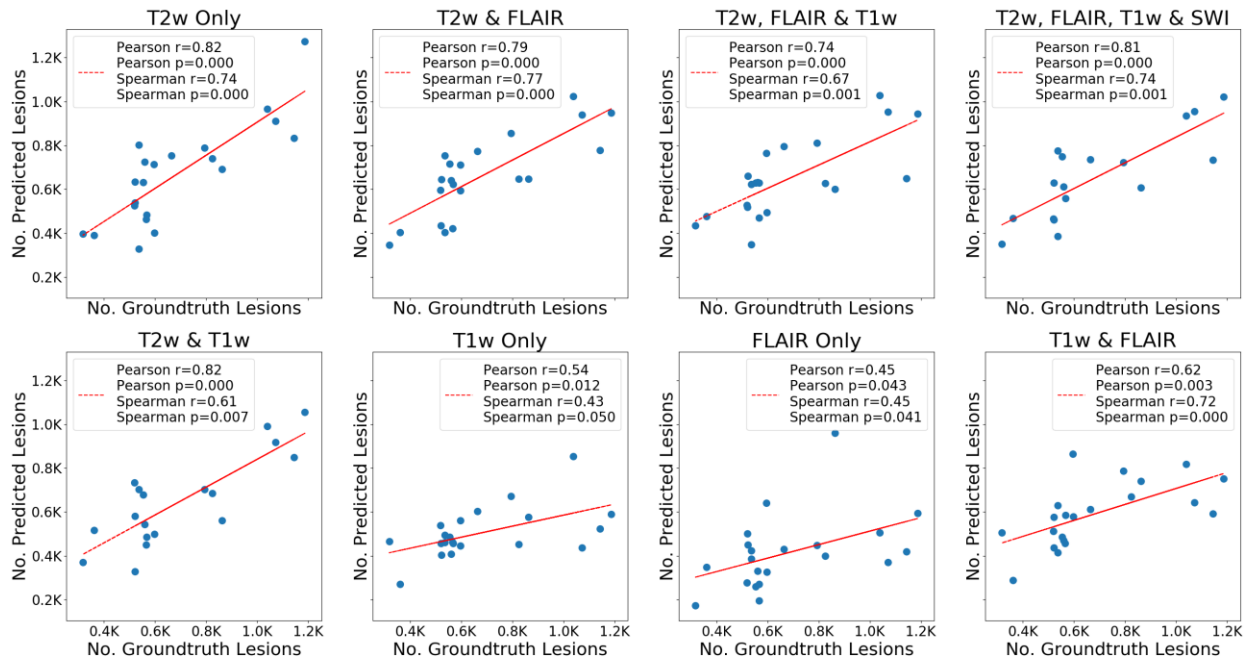


Fig. 3. Scatterplots of number of lesions/per case.

one-out cross-validation, we use data from 20 subjects for network training and data from one subject for testing. Also, from the 20 subjects used in training, four were used exclusively for within-training validation.

We aimed to train multiclass models, where predicted classes were background and ePVS, using the following combinations of imaging sequences: (1) T2w-only, (2) T2w and FLAIR, (3) T2w, T1w and FLAIR, (4) T2w, T1w, FLAIR, and SWI, (5) T2w and T1w, (6) FLAIR only, (7) T1w only, (8) T1w and FLAIR. Each 3-dimensional (3D) scan was cut into 2D axial slices, which underwent data augmentation through geometric operations such as flipping, translation, and rotation. For example, a single T2w MRI image having 96 axial slices resulted in 23880 axial slices after data augmentation. These augmented data were fed into the neural network as data samples.

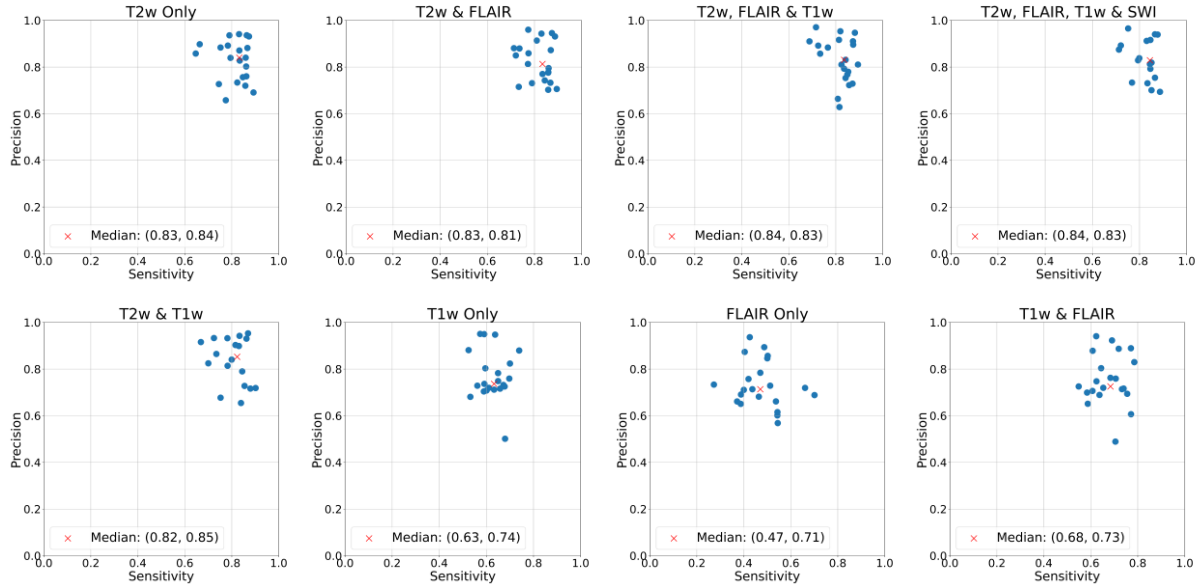


Fig. 4. Sensitivity vs precision.

3.3. Analysis of Detection Results

The accuracy of these models was based on three parameters: sensitivity S , precision P , and magnitude accuracy A , which are defined as

$$S = TP / (TP + FN), \quad P = TP / (TP + FP), \quad A = \sqrt{S^2 + P^2},$$

where TP is the number of true positives, FN is the number of false negatives, and FP stands for false positives.

We also selected metrics effective for small lesions like ePVS, where shape information and volume are essential. The ePVS could be as small as one voxel. The analysis included Bland-Altman plots and scatterplots of ePVS count and volumes (prediction vs. expert labeled data), as well as sensitivity and precision based on the center of mass of the lesions. We also assessed performance using intra-class correlation coefficients (ICC)³⁷, volumetric similarity³⁸, area

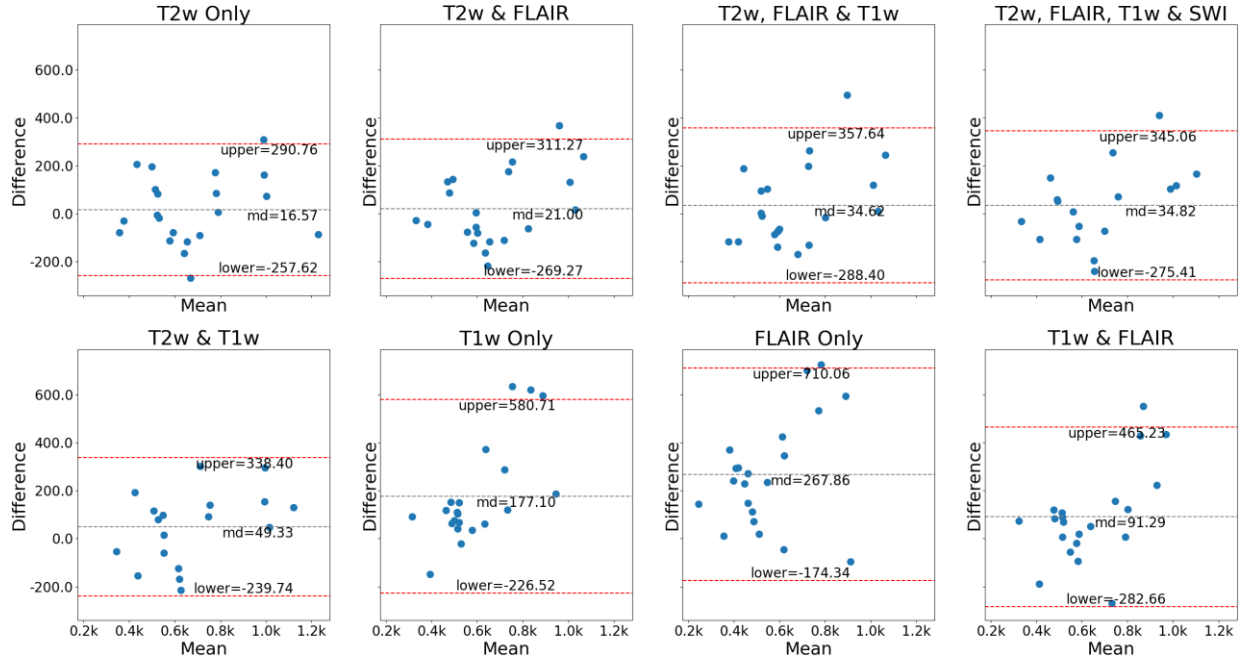


Fig. 5. Bland-Altman plot of number of lesions.

under the curve (AUC) from receiver operator curves, Hausdorff distance³⁹, and Mahalanobis distance⁴⁰. For ICC, we calculate the correlation between the total number of lesions of ground truth and that of the prediction, as well as the correlation between the total volumes of ground truth and that of the prediction. Hausdorff distance calculates the distance between two point sets that correspond to ground truth labels and segmentations, respectively, while Mahalanobis distance is a multivariate distance metric that measures the distance between a point and a distribution and is particularly effective for classification on highly imbalanced datasets. The mean metrics are obtained by averaging over subjects, e.g., suppose S_i is the sensitivity obtained by testing subject i ($i = 1, 2, \dots, 21$), then average sensitivity $\bar{S} = \frac{1}{21} \sum_{i=1}^{21} S_i$.

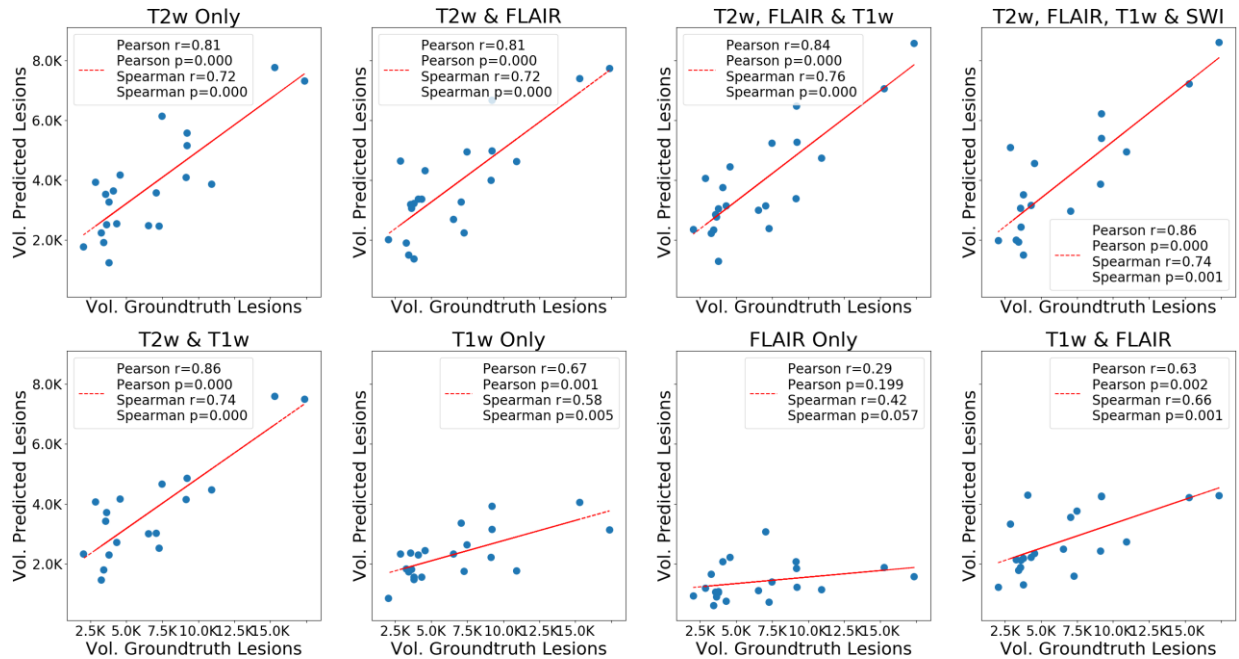


Fig. 6. Scatterplots of volume of lesions.

4. Results

The mean evaluation metrics with corresponding standard errors of all subjects, including sensitivity, precision, magnitude accuracy, ICC, volumetric similarity, AUC, Hausdorff distance, and Mahanabolis distance, are shown in Table 1. The results indicate that T2w MRI is the most informative, with the best performance of any single sequence and near-optimal for several measures. For most measures, the combination of T2w, FLAIR, T1w, and SWI achieved the best performance. Adding SWI to the combination of the other three sequences offered minimal overall gain but improved ICC.

Fig. 3 displays the correlations between the number of predicted lesions and that of ground-truth lesions. The highest correlations are achieved by using T2w. Fig. 4 plots the points located by pairs (S, P) from all the participants and indicates that by including T2w, FLAIR, and T1w the model could attain the highest magnitude accuracy, which is reflected by the distance

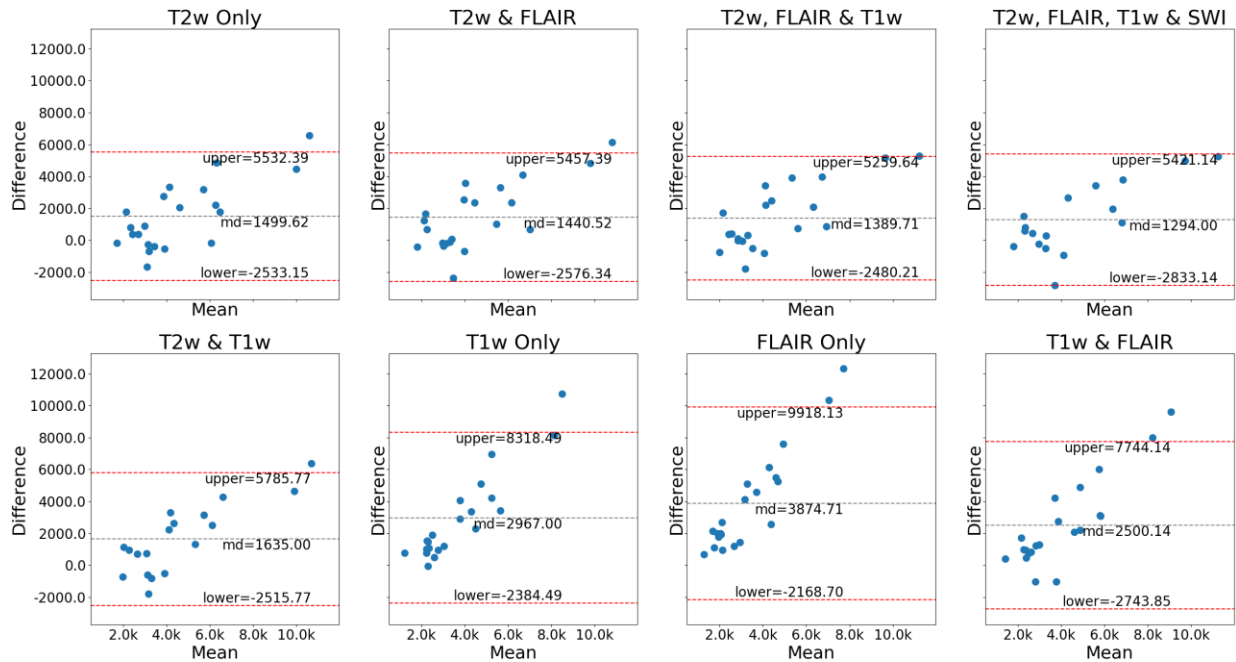


Fig. 7. Bland-Altman plot of volume of lesions.

between (\bar{S}, \bar{P}) and $(0, 0)$ in the figure, where \bar{S} and \bar{P} are the median sensitivity and median precision, respectively.

Fig. 5 shows the Bland-Altman plots of number of lesions, demonstrating that the mean difference between the prediction and the gold standard as well as the random fluctuations around the mean, reached the minimum when using T2w only and remained low when incorporating other sequences. Fig. 6 displays the correlations between the volume of predicted lesions and the volume of the ground truth, reaffirming the importance of using T2w for ePVS segmentation. Fig. 7 shows the Bland-Altman plots of lesion volumes, indicating that the combination of T2w, FLAIR, T1w, and SWI could attain better results than using FLAIR, T1w only since the mean difference and the fluctuations were minimal when combining T2w, T1w, FLAIR, and SWI, and were significantly smaller when T2w is included.

Table 1 - Subject-wise evaluation. The best scores are marked as red and the second best as blue.

Expts	Avg Sensitivity	Avg Precision	Avg Mag Accuracy	Avg Volumetric Similarity	Avg AUC	Average Hausdorff Distance	Average Mahanabolis Distance	ICC (#Lesions)	ICC (Volume)
T2w	0.81±0.01	0.83±0.02	1.16±0.02	0.81±0.03	0.72±0.01	1.41±0.08	0.17±0.02	0.83	0.59
2w+FLAIR	0.82±0.01	0.82±0.02	1.16±0.01	0.81±0.03	0.73±0.01	1.38±0.08	0.16±0.02	0.77	0.60
2w+FLAIR+T1w	0.82±0.01	0.83±0.02	1.17±0.01	0.82±0.03	0.74±0.01	1.27±0.07	0.17±0.02	0.70	0.63
2w+FLAIR+T1w+SWI	0.82±0.02	0.83±0.02	1.17±0.02	0.82±0.03	0.74±0.01	1.28±0.07	0.16±0.01	0.77	0.67
T2w+T1w	0.80±0.02	0.84±0.02	1.16±0.02	0.78±0.02	0.71±0.01	1.40±0.09	0.18±0.01	0.79	0.58
T1w	0.63±0.01	0.77±0.02	1.00±0.02	0.66±0.04	0.59±0.01	2.49±0.11	0.24±0.02	0.30	0.18
FLAIR	0.47±0.02	0.73±0.02	0.88±0.02	0.48±0.04	0.53±0.02	3.59±0.09	0.35±0.04	0.24	0.05
1w+FLAIR	0.68±0.02	0.75±0.02	1.02±0.02	0.71±0.03	0.61±0.01	2.30±0.11	0.23±0.02	0.50	0.25

Based on such observations, we can see that although T1 and FLAIR are more standard research sequences, ePVS ratings using these two sequences are not nearly as accurate as including T2w, and incorporating other sequences did not improve results significantly. However, using information from different modalities enables the model to effectively distinguish ePVS from mimics like white matter lesions and lacunes, as demonstrated in Fig. 8.

5. Discussion and Conclusions

Enlarged perivascular spaces (ePVS) are increasingly recognized as a subclinical biomarker for brain health and disease, including cerebrovascular disease, and therefore quantification is of interest to the research community. Manual quantification of individual ePVS is extremely time-consuming^{9,24}, operator-dependent, and may not accurately reflect the actual burden of ePVS. Data-driven automated systems, including deep learning models, provide a promising way to generate robust, reproducible, and rapid quantification of ePVS from brain MRI scans.

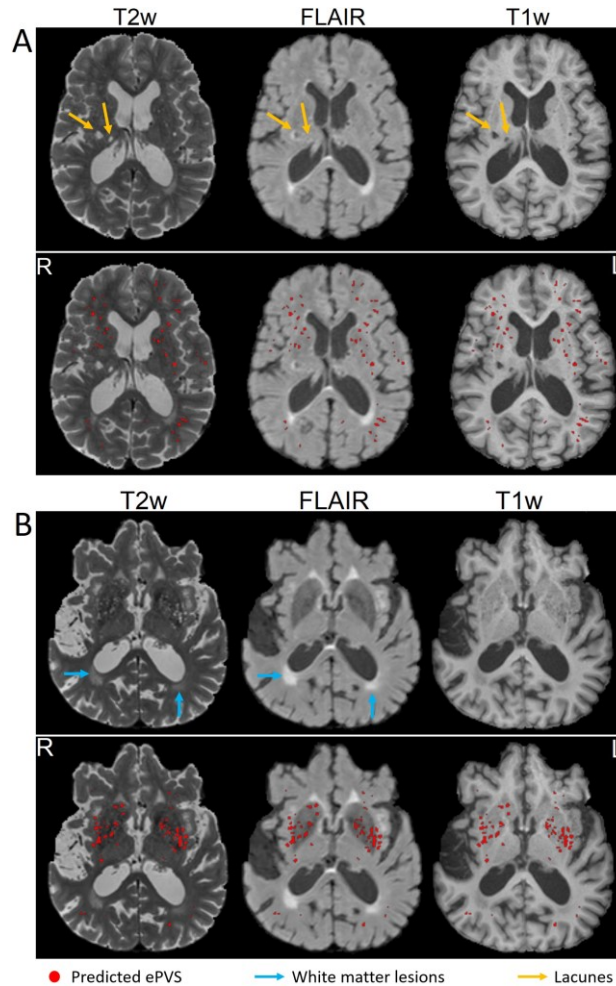


Fig. 8. An example of the predicted ePVS.

Automated ePVS quantification is challenging due to the existence of mimics like lacunes and white matter lesions, which may lead to false positive measurements. Furthermore, in many scenarios, the number of neuroimaging data samples could be insufficient to support data-driven systems. Such problems still remain in recently published deep learning methods.

In general, there are several limitations: 1) The issue of insufficient data samples is not addressed, and consequently there could be problems like overfitting; 2) It is still under question as to whether one single modality could be sufficiently informative for ePVS quantification; 3) The advantages of combining different sequences for the application is not investigated; 4)

Existing methods generally use 7T MRI while 3T data is more common in practice; 5) Existing methods were only applied to particular regions rather than the whole brain.

To address these issues, this study aims to fully exploit the informative 3T MRI data available by jointly utilizing different sequences and investigating the optimal strategy of fusing information from different sequences in the deep learning framework for ePVS segmentation, which could be applied to the whole brain. Specifically, since the number of data samples is often limited, it is of great importance to make full use of the data available, and the fusion of information from different sequences could be an effective solution. The deep learning model adopts a lightweight multi-channel variation of the U-Net tailored for the application. The experimental results demonstrate that the combination of T2w, FLAIR, T1w, and SWI leads to the best segmentation performance and that performance with T1w alone is worse than T2w alone for detecting ePVS. Our results suggest that if the quantification of ePVS is of interest, prospective research studies should include T2w imaging in a brain MRI protocol. T1w images, which are by far more prevalent in research studies due to their utility in brain tissue segmentation, should be expected to provide less accurate quantification of ePVS.

For regional evaluation, we derived several regions based on the existing MUSE segmentations, as shown in Fig. S1 of the supplementary material. Based on these regions, we did the same sensitivity and precision calculations for each individual region in all the experiments. The metrics, including mean sensitivity and precision, etc., are in Table S3 ~ S9 of the supplementary material. We can see that in the basal ganglia, the sensitivity and precision are high for all experiments, even when using only T1 or FLAIR. This suggests we can get reliable and accurate ePVS readings in the basal ganglia using only T1 and/or FLAIR. On the other hand, we see that the sensitivity and precision are poor in the hippocampus and temporal regions. This

is because of false positives due to the presence of blood vessels prevalent in those regions. Currently, the most clinically relevant regions for ePVS readings are the basal ganglia, centrum semiovale, and maybe the midbrain^{2,3}. So our experiments show that our models can make accurate predictions in the basal ganglia and the centrum semiovale, even when T2 is absent.

In conclusion, the proposed automated pipeline enables robust and time-efficient readings of ePVS from MR scans and demonstrates the importance of T2w MRI for ePVS detection and the insignificant benefit of using multimodal images. It may also provide a potential way to alleviate the issues brought about by the limitation of data samples. The automated pipeline will help in generating a rich variable set in MESA that will enable the examination of ePVS in relation to other risk factors. A limitation of the study is that manual ePVS segmentation from only one expert is available.

REFERENCES

-
1. Doubal FN, MacLulich AM, Ferguson KJ, Dennis MS, Wardlaw JM. Enlarged perivascular spaces on MRI are a feature of cerebral small vessel disease. *Stroke*. 2010;41(3):450-454.
 2. Wardlaw JM, Benveniste H, Nedergaard M, et al. Perivascular spaces in the brain: anatomy, physiology, and pathology. *Nature Reviews Neurology*. 2020;16(3):137-153.
 3. Wardlaw JM, Smith EE, Biessels GJ, et al. Neuroimaging standards for research into small vessel disease and its contribution to ageing and neurodegeneration. *The Lancet Neurology*. 2013;12(8):822-838.
 4. Potter GM, Doubal FN, Jackson CA, et al. Enlarged perivascular spaces and cerebral

-
- small vessel disease. *International journal of stroke*. 2015;10(3):376-381.
5. Hou Y, Park SH, Wang Q, et al. Enhancement of perivascular spaces in 7 T MR image using Haar transform of non-local cubes and block-matching filtering. *Scientific reports*. 2017;7(1):1-12.
 6. Potter GM, Chappell FM, Morris Z, Wardlaw JM. Cerebral perivascular spaces visible on magnetic resonance imaging: development of a qualitative rating scale and its observer reliability. *Cerebrovascular diseases*. 2015;39(3-4):224-231.
 7. Ballerini L, Lovreglio R, Hernández MdCV, et al. Perivascular spaces segmentation in brain MRI using optimal 3D filtering. *Scientific reports*. 2018;8(1):1-11.
 8. Zhang J, Gao Y, Park SH, Zong X, Lin W, Shen D. Structured learning for 3-D perivascular space segmentation using vascular features. *IEEE Transactions on Biomedical Engineering*. 2017;64(12):2803-2812.
 9. Wang X, Hernández MdCV, Doubal F, et al. Development and initial evaluation of a semi-automatic approach to assess perivascular spaces on conventional magnetic resonance images. *Journal of neuroscience methods*. 2016;257:34-44.
 10. Lian C, Zhang J, Liu M, et al. Multi-channel multi-scale fully convolutional network for 3D perivascular spaces segmentation in 7T MR images. *Medical image analysis*. 2018;46:106-117.
 11. Austin TR, Nasrallah IM, Erus G, et al. Association of Brain Volumes and White Matter Injury With Race, Ethnicity, and Cardiovascular Risk Factors: The Multi-Ethnic Study of Atherosclerosis. *Journal of the American Heart Association*. 2022:e023159.
 12. Bild DE, Bluemke DA, Burke GL, et al. Multiethnic study of atherosclerosis: objectives and design. *American journal of epidemiology*. 2002;156(9):871-881.

-
13. Olson JL, Bild DE, Kronmal RA, Burke GL. Legacy of MESA. *Global heart*. 2016;11(3):269-274.
 14. Burke G, Lima J, Wong ND, Narula J. The multiethnic study of atherosclerosis. *Global Heart*. 2016;11(3).
 15. Rashid T, Abdulkadir A, Nasrallah IM, et al. DEEPMIR: A DEEP neural network for differential detection of cerebral Microbleeds and IRon deposits in MRI. *Scientific Reports*. 2021.
 16. Hurtz S, Chow N, Watson AE, et al. Automated and manual hippocampal segmentation techniques: Comparison of results, reproducibility and clinical applicability. *NeuroImage: Clinical*. 2019;21:101574.
 17. Habes M, Erus G, Toledo JB, et al. White matter hyperintensities and imaging patterns of brain ageing in the general population. *Brain*. 2016;139(4):1164-1179.
 18. Habes M, Janowitz D, Erus G, et al. Advanced brain aging: relationship with epidemiologic and genetic risk factors, and overlap with Alzheimer disease atrophy patterns. *Translational Psychiatry*. 2016;6(4):e775-e775.
 19. Habes M, Pomponio R, Shou H, et al. The Brain Chart of Aging: Machine-learning analytics reveals links between brain aging, white matter disease, amyloid burden, and cognition in the iSTAGING consortium of 10,216 harmonized MR scans. *Alzheimer's & Dementia*. 2021;17(1):89-102.
 20. Liu H, Rashid T, Habes M. Cerebral Microbleed Detection Via Fourier Descriptor with Dual Domain Distribution Modeling. Paper presented at: 2020 IEEE 17th International Symposium on Biomedical Imaging Workshops (ISBI Workshops)2020.
 21. Liu H, Rashid T, Ware J, et al. Adaptive Squeeze-and-Shrink Image Denoising for

-
- Improving Deep Detection of Cerebral Microbleeds. Paper presented at: International Conference on Medical Image Computing and Computer-Assisted Intervention2021.
22. González-Castro V, Valdés Hernández MdC, Chappell FM, Armitage PA, Makin S, Wardlaw JM. Reliability of an automatic classifier for brain enlarged perivascular spaces burden and comparison with human performance. *Clinical Science*. 2017;131(13):1465-1481.
 23. Boespflug EL, Schwartz DL, Lahna D, et al. MR imaging–based multimodal autoidentification of perivascular spaces (mMAPS): automated morphologic segmentation of enlarged perivascular spaces at clinical field strength. *Radiology*. 2018;286(2):632-642.
 24. Ramirez J, Berezuk C, McNeely AA, Scott CJ, Gao F, Black SE. Visible Virchow-Robin spaces on magnetic resonance imaging of Alzheimer's disease patients and normal elderly from the Sunnybrook Dementia Study. *Journal of Alzheimer's Disease*. 2015;43(2):415-424.
 25. Sepehrband F, Barisano G, Sheikh-Bahaei N, et al. Image processing approaches to enhance perivascular space visibility and quantification using MRI. *Scientific reports*. 2019;9(1):1-12.
 26. Yin S, Peng Q, Li H, et al. Multi-instance deep learning with graph convolutional neural networks for diagnosis of kidney diseases using ultrasound imaging. Paper presented at: Uncertainty for Safe Utilization of Machine Learning in Medical Imaging and Clinical Image-Based Procedures2019.
 27. Mou C, Zhang J, Fan X, Liu H, Wang R. COLA-Net: Collaborative Attention Network for Image Restoration. *IEEE Transactions on Multimedia*. 2021.

-
28. Song Q, Liu H. Deep Gradient Prior Regularized Robust Video Super-Resolution. *Electronics*. 2021;10(14):1641.
 29. Boutinaud P, Tsuchida A, Laurent A, et al. 3D segmentation of perivascular spaces on T1-weighted 3 Tesla MR images with a convolutional autoencoder and a U-shaped neural network. *Frontiers in neuroinformatics*. 2021;15:29.
 30. Dubost F, Yilmaz P, Adams H, et al. Enlarged perivascular spaces in brain MRI: Automated quantification in four regions. *Neuroimage*. 2019;185:534-544.
 31. Sudre CH, Anson BG, Ingala S, et al. 3D multirater RCNN for multimodal multiclass detection and characterisation of extremely small objects. Paper presented at: International Conference on Medical Imaging with Deep Learning 2019.
 32. Jung E, Chikontwe P, Zong X, Lin W, Shen D, Park SH. Enhancement of perivascular spaces using densely connected deep convolutional neural network. *IEEE Access*. 2019;7:18382-18391.
 33. Avants BB, Tustison N, Song G. Advanced normalization tools (ANTs). *Insight j*. 2009;2(365):1-35.
 34. Doshi J, Erus G, Ou Y, et al. MUSE: MUlti-atlas region Segmentation utilizing Ensembles of registration algorithms and parameters, and locally optimal atlas selection. *Neuroimage*. 2016;127:186-195.
 35. Haacke EM, Mittal S, Wu Z, Neelavalli J, Cheng Y-C. Susceptibility-weighted imaging: technical aspects and clinical applications, part 1. *American Journal of Neuroradiology*. 2009;30(1):19-30.
 36. Ronneberger O, Fischer P, Brox T. U-net: Convolutional networks for biomedical image segmentation. Paper presented at: International Conference on Medical image computing

-
- and computer-assisted intervention 2015.
37. Bland J, Altman D. A note on the use of the intraclass correlation coefficient in the evaluation of agreement between two methods of measurement. *Computers in biology and medicine*. 1990;20(5):337-340.
 38. Ramaswamy Reddy A, Prasad E, Reddy L. Comparative analysis of brain tumor detection using different segmentation techniques. *International Journal of Computer Applications*. 2013;82(14):0975-8887.
 39. Rockafellar RT, Wets RJ-B. *Variational analysis*. Vol 317: Springer Science & Business Media; 2009.
 40. Xiang S, Nie F, Zhang C. Learning a Mahalanobis distance metric for data clustering and classification. *Pattern recognition*. 2008;41(12):3600-3612.

Deep Learning Based Detection of Enlarged Perivascular Spaces on Brain MRI

Supplementary Material

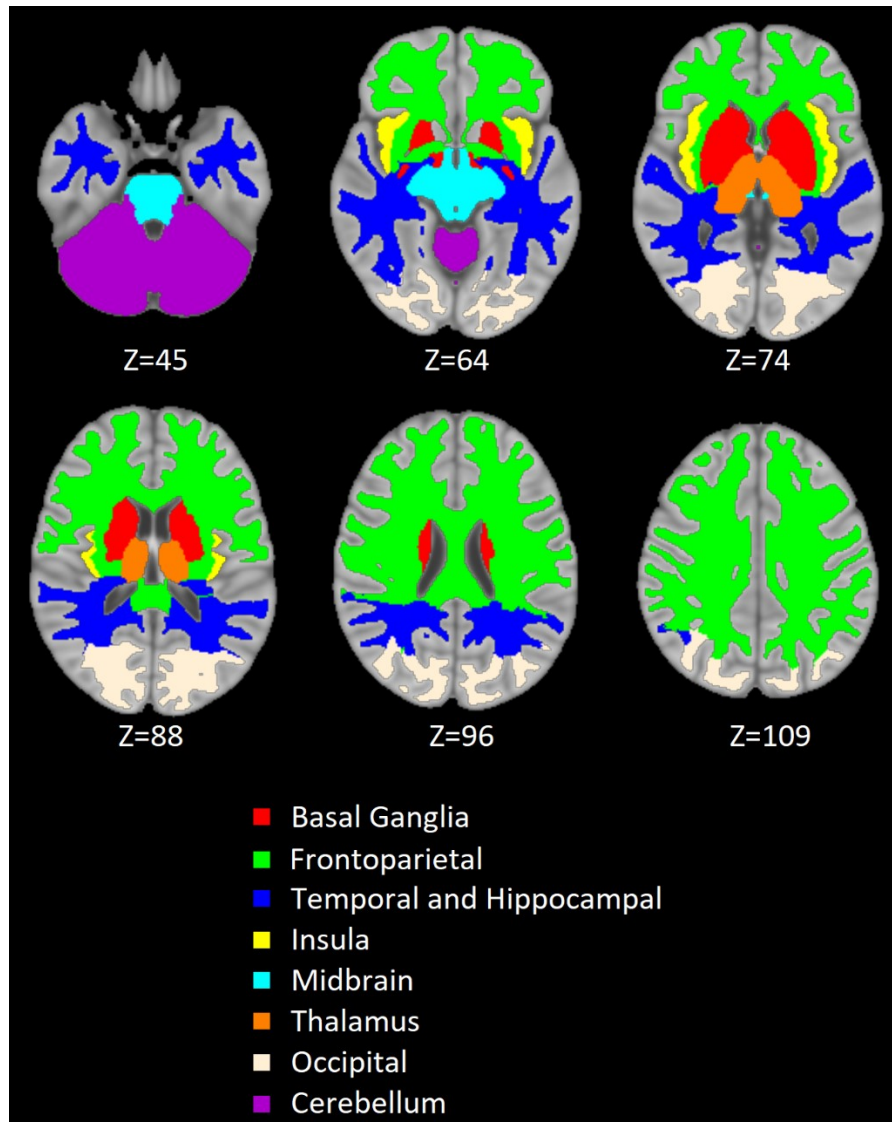


Fig. S1. Regions based on the existing MUSE segmentations.

Table S1 – MRI Scanner parameters.

MRI Modalities	TR (ms)	TE (ms)	FOV (mm)	Flip Angle	Slice Thickness (mm)	No of Slices	Matrix	Scan Duration
T1w	1900	2.93	250	9	1	176	256x256	4:26
T2w	3200	408	250	120	1	176	256x256	4:08
FLAIR	6000 (TI=2200)	289	250	120	1	160	258x221	4:14
SWI	35	7.5, 15, 22.5, and 30	256	15	1.5	96	256x192	6:00

Table S2 – Number and size of ePVS based on the expert labelled ground truth.

ID	EPVS Count	Total Voxels	Avg Voxels
Participant 1	554	2840	5.13
Participant 2	522	3641	6.98
Participant 3	318	2741	8.62
Participant 4	825	5982	7.25
Participant 5	536	2286	4.26
Participant 6	1072	8735	8.15
Participant 7	794	7357	9.27
Participant 8	1144	7303	6.38
Participant 9	863	5643	6.54
Participant 10	560	3020	5.39
Participant 11	596	3261	5.47
Participant 12	1187	13880	11.69
Participant 13	597	5232	8.76
Participant 14	521	2608	5.01
Participant 15	566	5819	10.28
Participant 16	664	7354	11.08
Participant 17	1039	12219	11.76
Participant 18	567	3448	6.08
Participant 19	519	2893	5.57
Participant 20	536	3019	5.63
Participant 21	361	1616	4.48

Table S3 - Subject-wise evaluation in the basal ganglia region. The best scores are marked as red and the second best as blue.

Expts	Avg Sensitivity	Avg Precision	Avg Mag Accuracy	Avg Volumetric Similarity	Avg AUC	Average Hausdorff Distance	Average Mahanabolis Distance	ICC (#ePVS)	ICC (Volume)
T2w	0.92	0.89	1.28	0.93	0.82	0.58	0.17	0.76	0.93
T2w+FLAIR	0.92	0.89	1.29	0.92	0.82	0.58	0.16	0.76	0.93
T2w+FLAIR+T1w	0.92	0.89	1.28	0.92	0.82	0.56	0.19	0.63	0.96
T2w+FLAIR+T1w+SWI	0.94	0.90	1.30	0.93	0.82	0.53	0.15	0.67	0.96
T2w+T1w	0.88	0.88	1.28	0.93	0.80	0.61	0.19	0.63	0.92
T1w	0.84	0.83	1.19	0.86	0.66	1.33	0.30	0.55	0.67
FLAIR	0.88	0.81	1.20	0.85	0.68	1.26	0.30	0.23	0.21
T1w+FLAIR	0.80	0.80	1.13	0.68	0.56	2.01	0.45	0.32	0.63

Table S4 - Subject-wise evaluation in the frontoparietal region. The best scores are marked as red and the second best as blue.

Expts	Avg Sensitivity	Avg Precision	Avg Mag Accuracy	Avg Volumetric Similarity	Avg AUC	Average Hausdorff Distance	Average Mahanabolis Distance	ICC (#ePVS)	ICC (Volume)
T2w	0.82	0.85	1.18	0.78	0.71	1.40	0.23	0.78	0.58
T2w+FLAIR	0.82	0.85	1.19	0.77	0.72	1.30	0.17	0.74	0.60
T2w+FLAIR+T1w	0.83	0.85	1.19	0.80	0.74	1.24	0.19	0.67	0.64
T2w+FLAIR+T1w+SWI	0.83	0.85	1.19	0.77	0.73	1.25	0.19	0.70	0.65
T2w+T1w	0.77	0.85	1.17	0.75	0.71	1.43	0.21	0.61	0.61
T1w	0.64	0.79	1.02	0.67	0.58	2.57	0.34	0.24	0.18
FLAIR	0.49	0.77	0.92	0.46	0.52	3.77	0.52	0.22	0.04
T1w+FLAIR	0.69	0.78	1.04	0.71	0.60	2.39	0.29	0.46	0.26

Table S5 - Subject-wise evaluation in the temporal and hippocampal region. The best scores are marked as red and the second best as blue.

Expts	Avg Sensitivity	Avg Precision	Avg Mag Accuracy	Avg Volumetric Similarity	Avg AUC	Average Hausdorff Distance	Average Mahanabolis Distance	ICC (#ePVS)	ICC (Volume)
T2w	0.78	0.78	1.11	0.79	0.72	1.78	0.25	0.87	0.75
T2w+FLAIR	0.78	0.77	1.11	0.77	0.72	1.83	0.23	0.83	0.73
T2w+FLAIR+T1w	0.78	0.78	1.11	0.80	0.74	1.62	0.24	0.80	0.75
T2w+FLAIR+T1w+SWI	0.76	0.78	1.10	0.77	0.73	1.77	0.26	0.78	0.69
T2w+T1w	0.73	0.80	1.11	0.77	0.70	1.86	0.27	0.84	0.72
T1w	0.54	0.68	0.88	0.65	0.58	3.45	0.39	0.40	0.30
FLAIR	0.33	0.63	0.72	0.40	0.52	5.02	0.53	0.18	0.07
T1w+FLAIR	0.59	0.67	0.90	0.70	0.60	3.19	0.37	0.44	0.40

Table S6 - Subject-wise evaluation in the insula region. The best scores are marked as red and the second best as blue.

Expts	Avg Sensitivity	Avg Precision	Avg Mag Accuracy	Avg Volumetric Similarity	Avg AUC	Average Hausdorff Distance	Average Mahanabolis Distance	ICC (#ePVS)	ICC (Volume)
T2w	0.47	0.63	0.86	0.55	0.62	4.62	1.59	0.80	0.43
T2w+FLAIR	0.55	0.68	0.95	0.52	0.60	7.65	1.37	0.80	0.40
T2w+FLAIR+T1w	0.60	0.71	0.98	0.58	0.64	5.02	1.29	0.77	0.25
T2w+FLAIR+T1w+SWI	0.63	0.69	1.04	0.58	0.64	3.55	1.06	0.78	0.28
T2w+T1w	0.47	0.70	0.92	0.55	0.60	9.00	1.91	0.84	0.22
T1w	0.39	0.53	0.72	0.54	0.56	6.50	3.20	0.38	0.06
FLAIR	0.34	0.53	0.70	0.41	0.51	9.78	14.35	0.03	0.01
T1w+FLAIR	0.38	0.49	0.68	0.48	0.55	7.06	3.36	0.07	-0.04

Table S7 - Subject-wise evaluation in the midbrain region. The best scores are marked as red and the second best as blue.

Expts	Avg Sensitivity	Avg Precision	Avg Mag Accuracy	Avg Volumetric Similarity	Avg AUC	Average Hausdorff Distance	Average Mahanobolis Distance	ICC (#ePVS)	ICC (Volume)
T2w	0.72	0.73	1.05	0.73	0.73	2.18	0.72	0.79	0.69
T2w+FLAIR	0.77	0.71	1.07	0.78	0.74	2.39	0.65	0.63	0.61
T2w+FLAIR+T1w	0.78	0.71	1.08	0.79	0.77	2.43	0.79	0.65	0.54
T2w+FLAIR+T1w+SWI	0.79	0.73	1.09	0.80	0.76	2.54	0.74	0.60	0.72
T2w+T1w	0.76	0.70	1.07	0.80	0.76	2.32	0.71	0.55	0.55
T1w	0.53	0.69	0.89	0.62	0.62	3.76	1.58	0.39	0.56
FLAIR	0.41	0.62	0.77	0.42	0.53	5.98	1.68	0.29	0.06
T1w+FLAIR	0.56	0.66	0.91	0.66	0.63	3.62	1.32	0.38	0.51

Table S8 - Subject-wise evaluation in the thalamus region. The best scores are marked as red and the second best as blue.

Expts	Avg Sensitivity	Avg Precision	Avg Mag Accuracy	Avg Volumetric Similarity	Avg AUC	Average Hausdorff Distance	Average Mahanobolis Distance	ICC (#ePVS)	ICC (Volume)
T2w	0.72	0.70	1.05	0.73	0.72	4.08	2.10	0.62	0.43
T2w+FLAIR	0.73	0.61	0.99	0.71	0.72	4.72	4.82	0.65	0.62
T2w+FLAIR+T1w	0.72	0.70	1.03	0.72	0.71	2.92	5.88	0.66	0.64
T2w+FLAIR+T1w+SWI	0.66	0.74	1.13	0.73	0.76	2.41	0.84	0.74	0.63
T2w+T1w	0.53	0.74	0.97	0.64	0.61	4.16	1.37	0.76	0.74
T1w	0.28	0.48	0.61	0.35	0.51	8.75	3.53	0.50	0.52
FLAIR	0.58	0.64	0.90	0.59	0.61	4.05	1.56	0.27	0.06
T1w+FLAIR	0.72	0.61	1.01	0.77	0.75	3.93	5.29	0.50	0.44

Table S9 - Subject-wise evaluation in the occipital region. The best scores are marked as red and the second best as blue.

Expts	Avg Sensitivity	Avg Precision	Avg Mag Accuracy	Avg Volumetric Similarity	Avg AUC	Average Hausdorff Distance	Average Mahanabolis Distance	ICC (#ePVS)	ICC (Volume)
T2w	0.71	0.76	1.06	0.70	0.70	3.65	0.55	0.87	0.68
T2w+FLAIR	0.70	0.72	1.03	0.68	0.70	3.69	0.63	0.78	0.76
T2w+FLAIR+T1w	0.68	0.68	0.98	0.63	0.68	4.24	0.57	0.74	0.83
T2w+FLAIR+T1w+SWI	0.49	0.64	0.82	0.59	0.57	4.70	0.71	0.80	0.85
T2w+T1w	0.21	0.49	0.54	0.39	0.51	9.49	1.23	0.80	0.76
T1w	0.53	0.59	0.82	0.69	0.58	5.20	0.70	0.50	0.30
FLAIR	0.67	0.74	1.02	0.71	0.69	3.87	0.57	0.16	0.05
T1w+FLAIR	0.65	0.70	0.98	0.67	0.69	4.10	0.53	0.58	0.50